



## City Research Online

### City, University of London Institutional Repository

---

**Citation:** Rahman, B. M., Kejalakshmy, N., Uthman, M., Agrawal, A., Wongcharoen, T. & Grattan, K. T. V. (2009). Mode degeneration in bent photonic crystal fiber study by using the finite element method. *Applied Optics*, 48(31), G131 - G138. doi: 10.1364/ao.48.00g131

This is the accepted version of the paper.

This version of the publication may differ from the final published version.

---

**Permanent repository link:** <https://openaccess.city.ac.uk/id/eprint/1222/>

**Link to published version:** <https://doi.org/10.1364/ao.48.00g131>

**Copyright:** City Research Online aims to make research outputs of City, University of London available to a wider audience. Copyright and Moral Rights remain with the author(s) and/or copyright holders. URLs from City Research Online may be freely distributed and linked to.

**Reuse:** Copies of full items can be used for personal research or study, educational, or not-for-profit purposes without prior permission or charge. Provided that the authors, title and full bibliographic details are credited, a hyperlink and/or URL is given for the original metadata page and the content is not changed in any way.

---

---

---

City Research Online:

<http://openaccess.city.ac.uk/>

[publications@city.ac.uk](mailto:publications@city.ac.uk)

---

# Mode degeneration in bent photonic crystal fiber study by using the finite element method

B. M. Azizur Rahman,<sup>1,\*</sup> Namassivayane Kejalakshmy,<sup>1</sup> Muhammad Uthman,<sup>1</sup>

Arti Agrawal,<sup>1</sup> Tiparatana Wongcharoen,<sup>2</sup> and Kenneth T. V. Grattan<sup>1</sup>

<sup>1</sup>School of Engineering and Mathematical Sciences, City University London,  
Northampton Square, London EC1V 0HB, UK

<sup>2</sup>Department of Electrical Engineering, Bangkok University, Bangkok, Thailand

\*Corresponding author: [B.M.A.Rahman@city.ac.uk](mailto:B.M.A.Rahman@city.ac.uk)

The development of highly dispersive lower and higher order cladding modes and their degeneration with respect to the fundamental core mode in a bent photonic crystal fiber is rigorously studied by use of the full-vectorial finite element method. It is shown that changes in the bending radius can modify the modal properties of large-area photonic crystal fibers, important for a number of potential practical applications.

## Introduction

Photonic crystal fibers (PCF) [1] are seen potentially as specialized optical waveguides due to the advantages arising from their inherent modal properties, such as controllable spot-size, birefringence and dispersion properties by tailoring their structural parameters. In their practical applications, such PCF go through bends, twists and stress. It is also well known that when a fiber is bent, the modal field shifts in the outward direction and suffers from radiation loss. One of the main disadvantages of standard silica fiber has been that the significant bending loss arises due to the low index contrast between the core and the cladding when compared to a PCF. However, sometimes a small bending radius may be unavoidable for any optical waveguide but on the other hand bending has been utilized to design functional devices such as ring resonators [2], arrayed waveguide filters [3], optical delay lines [4], S-bend attenuators [5] or to suppress higher order modes [6]. In this paper, work is reported on the rapid variation of key modal parameters which arises from the change in the coupling between the fundamental core mode and localized cladding mode between the air-holes by using a rigorous full-vectorial finite element method.

## Numerical Solutions

Various methods have been considered so far to study the modal characteristics of PCFs. One of the first methods used was the effective index method [10], which is a scalar field approach that treats the PCF as an equivalent step-index fiber and cannot yield the actual modal field profile and the modal birefringence of the PCF. The plane wave method (PWM) [11], a more widely used approach, needs a larger 'supercell' that demands periodicity of the PCF cladding and suffers from an inefficient computation time. The localized basis function method [12], the multipole method [13], and the supercell lattice method [14] are more effective methods than the PWM; but these methods have limitations in defining practical PCFs with a finite lattice period. These methods are unable to consider an arbitrary transverse variation of the PCF cross-section, such as is required in describing non-circular air-holes or non-identical multiple defects. On the other hand, more powerful and versatile finite difference method (FDM) [15], finite element method (FEM) [16] and beam propagation method (BPM) [18] are more effective when studying such complex microstructured fibers. A full-vectorial FEM [20] can be used efficiently in determining the quasi-TE and TM fundamental and higher order modes. A real value eigenvalue problem determined by the  $\mathbf{H}$  field formulation can be solved with higher computing efficiency, compared to other methods, in determining their important

modal properties such as the effective index, spot-size, dispersion, and cut-off of fundamental and higher order modes [21].

In the modal solution approach based on the FEM, the intricate cross-section of a PCF can be accurately represented by using nearly a million triangles of different shapes and sizes. The flexibility of irregular mesh makes the FEM preferable when compared to the FDM which not only uses inefficient regular spaced meshing, but also cannot represent adequately slanted or curved dielectric interfaces of the air-holes. The optical modes in a PCF with two dimensional confinement and high index contrast air/silica interfaces, are also hybrid in nature, with all six components of the  $\mathbf{E}$  and  $\mathbf{H}$  fields being present. Hence, only a vectorial formulation needs to be used to calculate accurately their modal solutions. The  $\mathbf{H}$  field formulation with the augmented penalty function technique is given below [20]:

$$\omega^2 = \frac{\left( \int (\nabla \times \bar{\mathbf{H}})^* \cdot \hat{\epsilon}^{-1} (\nabla \times \bar{\mathbf{H}}) d\Omega \right) + \left( \int (\eta/\epsilon_0) (\nabla \cdot \bar{\mathbf{H}})^* (\nabla \cdot \bar{\mathbf{H}}) d\Omega \right)}{\int \bar{\mathbf{H}}^* \cdot \hat{\mu} \bar{\mathbf{H}} d\Omega} \quad (1)$$

where  $\bar{\mathbf{H}}$  is the full-vectorial magnetic field,  $\hat{\epsilon}$  and  $\hat{\mu}$  are the permittivity and permeability respectively of the waveguide,  $\epsilon_0$  is the permittivity of the free-space,  $\omega^2$  is the eigenvalue, where  $\omega$  is the angular frequency of the wave and  $\eta$  is a dimensionless parameter used to impose the divergence-free condition of the magnetic field in a least squares sense.

To study arbitrary bends, various numerical methods have been developed and used to simulate the light propagation in bent waveguides with the aim of characterizing the bending, transition and polarization losses. The conformal transformation [22] has most widely been used to represent such bent waveguides by converting a curved dielectric waveguide to its equivalent straight waveguide with a modified index profile. The coordinate transformation allows a bent optical waveguide in the x-plane to be represented by an equivalent straight waveguide with modified refractive index distribution,  $n_{\text{eq}}(x,y)$

$$n_{\text{eq}}(x, y) = n(x, y) \left( 1 + \frac{x}{R} \right) \quad (2)$$

where  $n(x,y)$  is the original refractive index profile of the bent waveguide,  $n_{\text{eq}}(x,y)$  is the equivalent index profile of a straight guide,  $R$  is the radius of the curvature and  $x$  is the distance from the centre of the waveguide. Subsequently, the straight waveguide with a transformed index profile can be analysed by a number of modal solution techniques, such as the eigenmode expansion [23], the methods of lines [24], the FDM [26], the variational method [28], the matrix method [29], the WKB analysis [30], and the FEM [32,33]. The FEM has also been employed by using cylindrical co-ordinate with  $\mathbf{E}$  field [35] and the equivalent anisotropic refractive index approaches [36]. The beam propagation approach [37, 38] has been used successfully, but this approach makes the problem 3-dimensional with additional computational costs. Similarly the finite-difference time-domain (FDTD) [40] approach has also been used, which is more computer intensive than the modal solution or the BPM approaches.

In the original  $\mathbf{H}$ -field formulation [20], which considered a real eigenvalue equation, the PML [41] can be introduced around the orthodox computation window. The PML layer allows the electromagnetic waves to leak out of bent waveguides and avoids the reflection at the hard boundary of the orthodox computational window by using a slowly varying complex

refractive index profile. This allows the calculation of power loss out of the computation window but the introduction of the complex refractive index in the PML region also modifies the real eigenvalue to a complex eigenvalue equation. The modal loss value is calculated from the imaginary part ( $\alpha$ ) of the complex propagation constant  $\gamma = \beta + j\alpha$ . The width of PML layer has been chosen such that the modal solutions are stable with respect to the variations of the PML and the refractive indices of the local elements in the PML layer are matched with the local refractive indices at the edge of the cladding. Only one-half of the PCF cross section is considered here as the existing one-fold mirror symmetry of a bent PCF has been exploited.

## Results

In this study, silica photonic crystal fiber with air-holes arranged in a triangular lattice is considered, with the diameter of air-hole denoted by  $d$  and distance between two air-holes denoted by  $\Lambda$ . The refractive index of silica is taken as 1.444 at the operating wavelength of  $1.55 \mu\text{m}$ . A PCF can support two fundamental  $H^y_{11}$  (quasi-TE) and  $H^x_{11}$  (quasi-TM) modes and for higher  $\Lambda$  and  $d/\Lambda$  values, a PCF can also support additional higher order modes of a given polarization.

It is well known that such PCF suffers from leakage loss as the modal index is lower than the refractive index of the outer cladding silica region. This leakage loss can be reduced by increasing the number of air-hole rings or considering a well confined mode operating the far away from its cutoff condition. It is also well known that optical waveguides suffer from increased bending loss as its bending radius is reduced. The variation of the total loss for the fundamental quasi-TM ( $H^x_{11}$ ) mode with the bending radius,  $R$ , for three different pitch values, are shown in Fig. 1. In this case the  $d/\Lambda$  is taken to be constant and equal to 0.5. For a lower pitch length,  $\Lambda = 1.6 \mu\text{m}$ , the bending loss increases monotonically as the bending radius is reduced. However, in this case as leakage loss (for straight waveguide or when  $R$  is very large) is also high as the PCF is operating close to its modal cutoff. PCF with such a smaller pitch length is mostly not preferred due to their higher leakage losses. As the pitch length is increased, for  $\Lambda = 2.6 \mu\text{m}$ , the leakage loss reduced by three order of magnitude (at  $R = 10^4 \mu\text{m}$ , total loss contains mainly the leakage loss as the pure bending loss is nearly zero). For this case, as the bending radius is reduced, progressively the bending loss increases and as a result the total loss also increases. It can be noted that increases in the bending loss with the bending radius is more rapid as this is reduced, compared to the case with a lower pitch length,  $\Lambda = 1.6 \mu\text{m}$ . At a lower bending radius, this also shows a non-monotonic nature with oscillations in the total loss values. In these cases, it has been observed that the modal and leakage properties of both the quasi-TE and TM modes are almost similar along with the transition in their loss properties also at similar locations. When the pitch length is increased further,  $\Lambda = 5.0 \mu\text{m}$ , the leakage loss is significantly reduced to  $10^{-3}$  dB/m, and such a PCF with a larger dimension is often preferred. In this case, as the bending radius is reduced the total loss value increases rapidly and for some fixed radius values this value can even be higher than that of a PCF with a lower pitch value. However, in this case with a larger  $\Lambda$ , the oscillations in the loss values are more frequent and appear to be random in nature. Similar features have also been observed experimentally [x].

To study this particular feature more closely, a smaller bending radius range is further expanded with many additional simulated results in that region. Variation of the effective

index for the quasi-TM mode with the bending radius is shown in Fig.2. In this region, two distinct modes can easily be identified (their field profiles are shown later on). The solid line represents the first,  $H_{11}^x$  eigenmode, with a higher effective index and that of the second eigenmode,  $H_2^x$ , shown by a dashed line has a lower effective index for the range of bending radius shown here. In a way similar to the formation of the even and odd-like supermodes of two nonidentical coupled waveguides [7], these two curves never cross each other but these two modes go through a transition near  $R \sim 1445 \mu\text{m}$ , when they are phase matched. The horizontal sections of these two lines represent the  $H_{11}^x$  core mode confined at the center of the PCF. The slanted line represents a highly dispersive  $H_{c1}^x$  cladding mode, which is located at the right side of the core and between the two air-holes for a bent PCF. This cladding mode has a smaller core area but with a progressively higher local equivalent refractive index value as the bending radius is reduced. For a specific bending radius the effective index of the cladding mode becomes equal to that of the core mode and they degenerate. It should be noted that the dispersion properties of the TE and TM polarized modes for both the core and cladding modes are similar.

The loss values for these first  $H_{11}^x$  and second  $H_2^x$  modes are shown in Fig.3 by a solid and a dashed line, respectively. Part of these two curves form the lower section, which shows the loss values of the  $H_{11}^x$  core mode is around 100 dB/m (U:check it). On the other hand, the upper lines represent  $H_{c1}^x$  cladding modes with significantly higher loss values, around 12000 dB/m. However, these two curves also go through a transition near  $R \sim 1450 \mu\text{m}$ , similar as the effective index curves shown in Fig.2. It can be observed that the upper curve shows a local minimum near the mode degeneration point as being mixed with a less lossy  $H_{11}^x$  core mode. Similarly loss value of the lower curve also peaks near the resonance as being mixed with a highly lossy cladding mode. This local peak was clearly shown in Fig.1 for  $\Lambda = 5 \mu\text{m}$  around  $R = 1445 \mu\text{m}$ .

Variation of the  $H_x$  field for the  $H_{11}^x$  core mode along the center of the guide in the x-direction is shown in Fig.4 when  $R = 1480 \mu\text{m}$ . It can be observed that field is predominantly confined at the center of the PCF core, however, its maximum value is shifted slightly right of the waveguide center, shown by an arrow. Two local peaks are also visible located in the silica bridge region between the first and second air-hole rings and the 2<sup>nd</sup> and 3<sup>rd</sup> air-hole rings (shown as 1, 2 and 3), respectively. These peaks are only visible on the right of the core, not on the left side, as due to the conformal transformation, higher local equivalent index value allows such local modes to be formed on the right side of the core. Its spot-size is  $\text{xxx} \mu\text{m}^2$ , (U: give me the value) where the spot-size is defined as the area with more than  $1/e^{\text{th}}$  of the maximum field intensity.

At this particular bending radius,  $R = 1460 \mu\text{m}$ , a local cladding mode also exists with its effective index slightly lower than the  $H_{11}^x$  core mode. The 2-D  $H_x$  field contour for this  $H_{c1}^x$  cladding mode is shown in Fig.5. The location of the air-hole positions are shown by circles. It can clearly be observed that this cladding mode is formed in between the air-holes of the second and third rings. The spot-size area of this mode is significantly smaller ( $\sigma = \text{xx} \mu\text{m}^2$ ) (U: give me the value) as being restricted to a smaller silica bridging region but this mode is highly dispersive with a higher loss value.

When the bending radius is reduced below the degeneration point ( $R < 1445 \mu\text{m}$ ) effective index of the cladding mode becomes higher than that of the  $H_{11}^x$  core mode and the eigenvalues change their positions. The 3-D  $H_x$  field profile of the  $H_{11}^x$  core mode, when  $R = 1430 \mu\text{m}$ , is shown in Fig. 6. The local peaks on the right of the main peak are visible.

However, it can be observed that the sign of second peak in the cladding area is negative, which is also an indication of the change in mode order.

The 3-D  $H_x$  field profile of the  $H_{c1}^x$  cladding mode, when  $R = 1430 \mu\text{m}$ , is shown in Fig.7. Its narrower peak in between two air-holes (marked by 1 and 2) is clearly visible. Besides that, one local peak in the core region and another between the 2<sup>nd</sup> and 3<sup>rd</sup> air-hole rings are also visible.

It has been mentioned that the modal properties of the quasi-TM and TM modes were almost identical as the original straight PCF has a 6-fold rotational symmetry, before the bending is considered. In Fig.1, it was also noted that bending loss curve for  $\Lambda = 5 \mu\text{m}$ , showed several local perturbations. To study this more thoroughly, the bending radius is further reduced and the variation of the effective index values for the quasi-TE core and cladding modes are shown in Fig. 8. The effective index variation of the first  $H_{11}^y$  and second  $H_{22}^y$  modes are shown by a dashed and a solid line. It can be noted that the effective index of the fundamental core mode is higher than that shown in Fig.2, as bending radius is now significantly reduced. Similar as shown in Fig.2, these two effective index curves do not cross each other but transforms from the  $H_{11}^y$  core mode to the  $H_{c2}^y$  cladding mode or vice versa around  $R \sim 833 \mu\text{m}$ . Lower bending radius further increases the local refractive index on the right-side of the PCF center. The dispersion slope of the  $H_{c2}^y$  cladding mode is also higher in this case than that of the  $H_{c1}^x$  cladding mode.

Variation of the total loss values for the  $H_{11}^y$  core and  $H_{c2}^y$  cladding modes are shown in Fig.9. In this case, the core mode with a lower loss value transforms to higher loss cladding mode near the degeneration position. In this case the  $H_{11}^y$  cladding mode has a higher loss value than that of the  $H_{11}^x$  core mode around  $R \sim 1445 \mu\text{m}$ , since the bending radius is now significantly reduced. Its loss value also peaks near the degeneration point,  $R \sim 833 \mu\text{m}$ , as being mixed with a higher loss cladding mode. Similarly loss value of the cladding mode is reduced near the degeneration as being mixed with a lower loss core mode.

To understand the modal properties of this cladding mode at the lower bending radius range, the corresponding field plots are shown in Fig.10. The  $H^y$  field profile along the x-axis for the  $H_{11}^y$  core mode is shown in Fig.10, when  $R = 840 \mu\text{m}$ , just right of degeneration point is shown in Fig.10. The existence of a second peak in-between the first and second air-hole rings is clearly visible. In this case, the secondary peak is of a higher magnitude as the local equivalent refractive index is much higher due to a smaller bending radius being considered here. The  $H_y$  field profile of the  $H_{11}^y$  core mode at  $R = 830 \mu\text{m}$ , just left of the degeneration point is shown in Fig.11. In this case, the secondary peaks are also clearly visible. However, the change in its sign indicate that this mode is now a higher order mode, as its eigenvalue position has been shifted by the cladding mode.

The 2-D  $H_y$  contour of the  $H_{c2}^y$  cladding mode is shown in Fig.12. The locations of the air-holes are also shown by circles. It can be clearly observed that modal field is confined in the silica bridge region, between the first and second air-hole rings. It can also be noticed that the field spreads to link three silica bridging areas. However, one feature is very clear that this is a higher order cladding mode with its two positive and negative peaks shown by different colored contours. It should also be noted that local equivalent index value in between first and second air-hole rings would be lower than that of the between second and third air-hole rings. Thus, this cladding mode, also being a higher order mode, its effective index is significantly lower (compared to  $H_{c1}^x$  shown in Fig.5) for a larger bending radius. Hence, its effective

index value only crosses that of the fundamental core mode at a much lower bending radius, when this value is increased significantly.

## Conclusions

The above figures clearly show the origin of localised cladding modes in the silica bridging regions in-between the air-holes. As these areas are smaller than the PCF core (where an air-hole is missing), for a straight PCF these modes with lower effective indices do not interact with the PCF core mode. However, for a bent PCF, as the local equivalent index is increased, the dispersion slopes of these modes are higher and for smaller bending radii they can be phase matched to the core mode to form coupled supermodes. This mode degeneration cause mixing of these modes, formation of the supermodes and transom for one mode to another. These cause rapid changes in their modal properties, the effective index, spot-size and bending loss values. A higher pitch value or larger  $d/\Lambda$  ratio increases the silica bridging regions and such mode degeneration would appear at a higher bending radius, as often encountered in practical applications. In these cases, the mode degeneration appears more frequently and shows as noisy loss various in experimental measurements [x, y].

The origin of these fundamental and higher order cladding modes and coupling to core mode can effect the design of various PCF based applications. Study of this mode degeneration gives insight to the practical application of PCF and their handing during their real world applications. This understanding can also be useful in the study of PCF-based devices, exploiting bending loss, such as effectively single mode waveguide with differential modal losses and single polarization waveguide with highly differential polarization dependent bending losses, or in the design of optical attenuators.

## References

- [1] P. St. J. Russell, 'Photonic-crystal fibers,' *J. Lightwave Technol.* **24**, 4729-4749 (2006).
- [2] B. E. Little, S. T. Chu, H. A. Haus, J. Foresi, and J. P. Laine, "Microring resonator channel dropping filters," *J. Lightwave Technol.* **15**, 998-1005 (1997).
- [3] M. Zirngibl, C. H. Joyner, L. W. Stulz, Th. Gaiffe, and C. Dragone, "Polarization independent 8x8 waveguide grating multiplexers on InP," *Electron. Lett.* **29**, 201-202 (1993).
- [4] R. R. Hayes, and D. Yap, "GaAs spiral optical waveguides for delay-line applications," *J. Lightwave Technol.* **11**, 523-528 (1993).
- [5] X. Jiang, W. Qi, H. Zhang, Y. Tang, Y. Hao, J. Yang, and M. Wang, "Loss crosstalk 1x2 thermo-optic digital optical switch with integrated S-bend attenuator", *IEEE Photonics Technol. Lett.* **18**, 610-612 (2006).
- [6] K. Saitoh, N. J. Florous, M. Koshiba, and M. Skorobogatiy, "Design of narrow band-pass filters based on the resonant-tunneling phenomenon in multi-core photonic crystal fibers," *Opt. Express* **13**, 10327-10335 (2005)
- [7] K. Iizawa, S. K. Varshney, Y. Tsuchida, K. Saitoh, and M. Koshiba, "Bend-insensitive lasing characteristics of singlemode, large-mode-area Ytterbium-doped photonic crystal fiber," *Opt. Express* **16**, 579-591 (2008).
- [8] M. van Eijkelenborg, J. Canning, T. Ryan, and K. Lyytikainen, "Bending-induced colouring in a photonic crystal fibre," *Opt. Express* **7**, 88-94 (2000).
- [9] J. Olszewski, M. Szpulak, and W. Urbańczyk, "Effect of coupling between fundamental and cladding modes on bending losses in photonic crystal fibers," *Opt. Express* **13**, 6015-6022 (2005)
- [10] J. C. Knight, T. A. Birks, P. St. J. Russell, and J. P. de Sandro, "Properties of photonic crystal fiber and the effective index model," *J. Opt. Soc. Am. A* **15**, 748-752 (1998).



- [11] J. Arriaga, J. C. Knight and P. St. J. Russell, "Modeling the propagation of light in photonic crystal fibers," *Physica D - Nonlin. Phenomena* **189**, 100-106 (2004).
- [12] T. M. Monro, D. J. Richardson, N. G. R. Broderick and P. J. Bennett, "Holey Optical Fibers: An Efficient Modal Model," *J. Lightwave Technol.* **17**, 1093-1102 (1999).
- [13] T. P. White, R. C. McPhedran, C. M. de Sterke, L. C. Botten, and M. J. Steel, "Confinement losses in microstructured optical fibers," *Opt. Lett.* **26**, 1660-1662 (2001)
- [14] W. Zhi, R. Guobin, L. Shuqin, and J. Shuisheng, "Supercell lattice method for photonic crystal fibers," *Opt. Express* **11**, 980-991 (2003).
- [15] J. Riishede, N. A. Mortensen and J. Lægsgaard, "A 'poor man's approach' to modelling micro-structured optical fibres," *J. Optics A- Pure and Appl. Optics* **5**, 534-538 (2003).
- [16] B. M. A. Rahman, A. K. M. S. Kabir, M. Rajarajan and K. T. V. Grattan, "Finite element modal solutions of planar photonic crystal fibers with rectangular air-holes," *Opt. and Quantum Electron.* **37**, 171-183 (2005).
- [17] .
- [18] F. Fogli, L. Saccomandi, P. Bassi, G. Bellanca, and S. Trillo, "Full vectorial BPM modeling of index-guiding photonic crystal fibers and couplers," *Opt. Express* **10**, 54-59 (2002).
- [19] .
- [20] B. M. A. Rahman and J. B. Davies, "Finite-element solution of integrated optical waveguides," *J. Lightwave Technol.* **2**, 682-688 (1984).
- [21] N. Kejalakshmy, B.M.A. Rahman, A. K. M. S. Kabir, M. Rajarajan, and K.T.V. Grattan, "Single mode operation of photonic crystal fiber using a full vectorial finite element method", *Photonic Crystal Fibers*. Edited by Kalli, Kyriacos. Proceedings of the SPIE **6588** 65880T (2007).
- [22] M. Heiblum and J. H. Harris, "Analysis of curved optical waveguides by conformal transformation," *IEEE J. Quantum Electron.* **11**, 75-83 (1975).
- [23] P. Bienstman, E. Six, M. Roelens, M. Vanwolleghem, and R. Baets, "Calculation of bending losses in dielectric waveguides using eigenmode expansion and perfectly matched layers," *IEEE Photon. Technol. Lett.* **14**, 164-166 (2002).
- [24] J. Gu, P. Besse and H. Melchior, "Novel method for analysis of curved optical rib-waveguides," *Electron. Lett.* **25**, 278-280 (1989).
- [25] .
- [26] S. Kim and A. Gopinath, "Vector analysis of optical dielectric waveguide bends using finite-difference method," *J. Lightwave Technol.* **14**, 2085-2092 (1996).
- [27] .
- [28] F. Wassmann, "Modal field analysis of circularly bent single-mode fibers," *J. Lightwave Technol.* **17**, 957-968 (1999).
- [29] K. Thyagarajan, M. R. Shenoy, and A. K. Ghatak, "Accurate numerical method for the calculation of bending loss in optical waveguides using a matrix approach," *Opt. Lett.* **12**, 296-298 (1987).
- [30] W. Berglund and A. Gopinath, "WKB analysis of bend losses in optical waveguides," *J. Lightwave Technol.*, **18**, 1161-1166 (2000).
- [31] .
- [32] T. Yamamoto and M. Koshiha, "Numerical analysis of curvature loss in optical waveguides by the finite-element method", *J. Lightwave Technol.* **11**, 1579-1583 (1993).
- [33] K. Saitoh, Y. Tsuchida, M. Koshiha, and N. A. Mortensen, "Endlessly single-mode holey fibers: the influence of core design," *Opt. Express* **13**, 10833-10839 (2005).
- [34] R. Jedidi and R. Pierre, "High-order finite-element method for the computation of bending loss in optical waveguides," *J. Lightwave Technol.*, **25**, 2618-2630 (2007).

- [35] Y. Tsuji and M. Koshiba, "Complex modal analysis of curved optical waveguides using a full-vectorial finite element method with perfectly matched layer boundary conditions," *Electromagn.*, **24**, 39-48 (2004).
- [36] R. T. Schermer and J. H. Cole, "Improved bend loss formula verified for optical fiber by simulation and experiment," *IEEE J. Quantum Electron.* **43**, 899-909 (2007).
- [37] R. Baets and P. E. Lagasse, "Loss calculation and design of arbitrarily curved integrated-optic waveguides," *J. Opt. Soc. Am.*, **73**, pp.177-182 (1983).
- [38] M. Rajarajan, S. S. A. Obayya, B. M. A. Rahman, K. T. V. Grattan, and H. A. El-Mikathi, "Characterization of low-loss waveguide bends with offset optimisation for compact photonic integrated circuits," *IEE Proc. Optoelectronics* **147**, 382-388 (2000).
- [39] .
- [40] N. H. Vu, I. Hwang, and Y. Lee, "Bending loss analyses of photonic crystal fibers based on the finite-difference time-domain method," *Opt. Lett.* **33**, 119-121 (2008).
- [41] F. L. Teixeira and W. C. Chew, "General closed-form PML constitutive tensors to match arbitrary bianisotropic and dispersive linear media," *IEEE Microwave and Guided Wave Letters* **8**, 223-225 (1998).
- [42] A. Taflove and S.C. Hagness, *Computational Electrodynamics*, (Artech House Publishers, 2000).
- [43] N. A. Mortensen, "Effective area of photonic crystal fibers," *Opt. Express* **10**, 341-348 (2002).

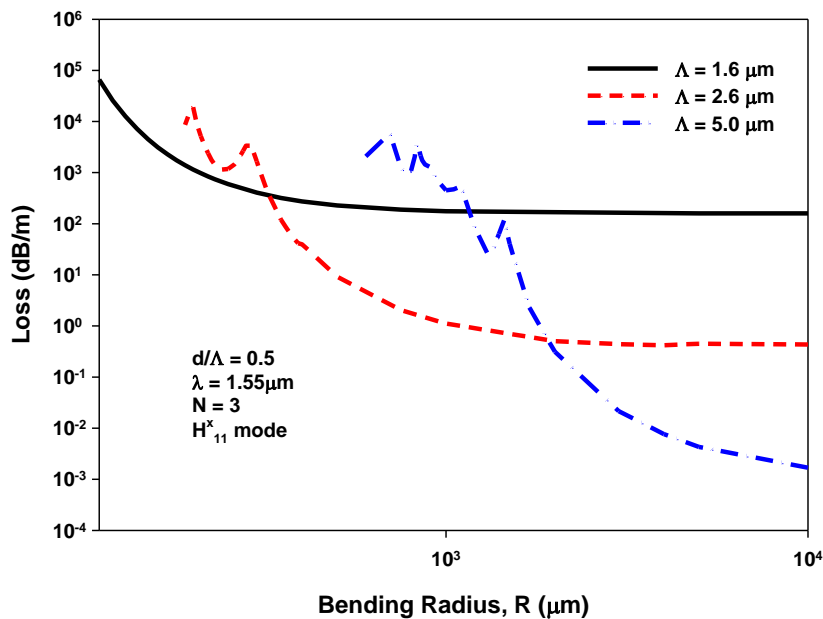


Fig. 1. Variation of the total losses with the bending radius, R for the quasi-TM modes.

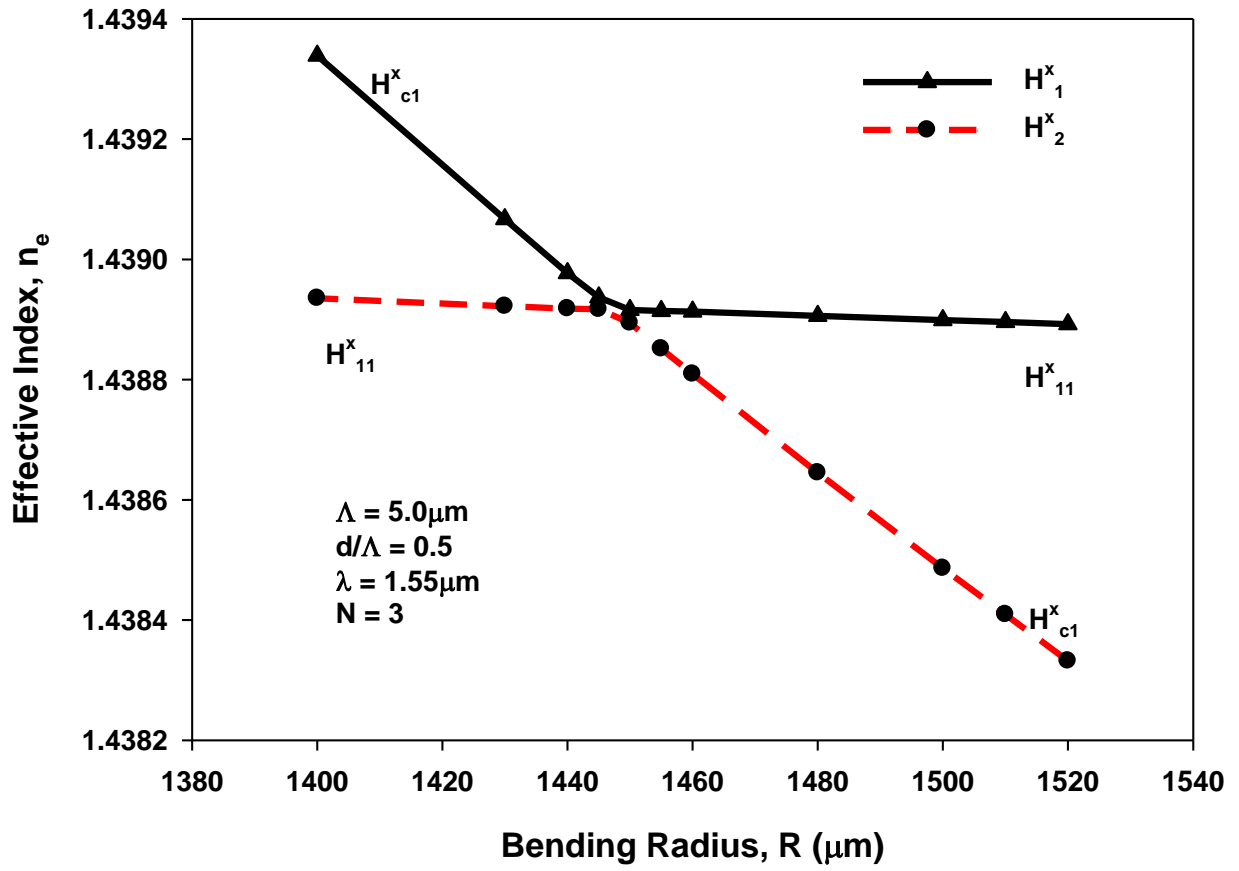


Fig. 2. Variation of the effective indices with the bending radius,  $R$ .

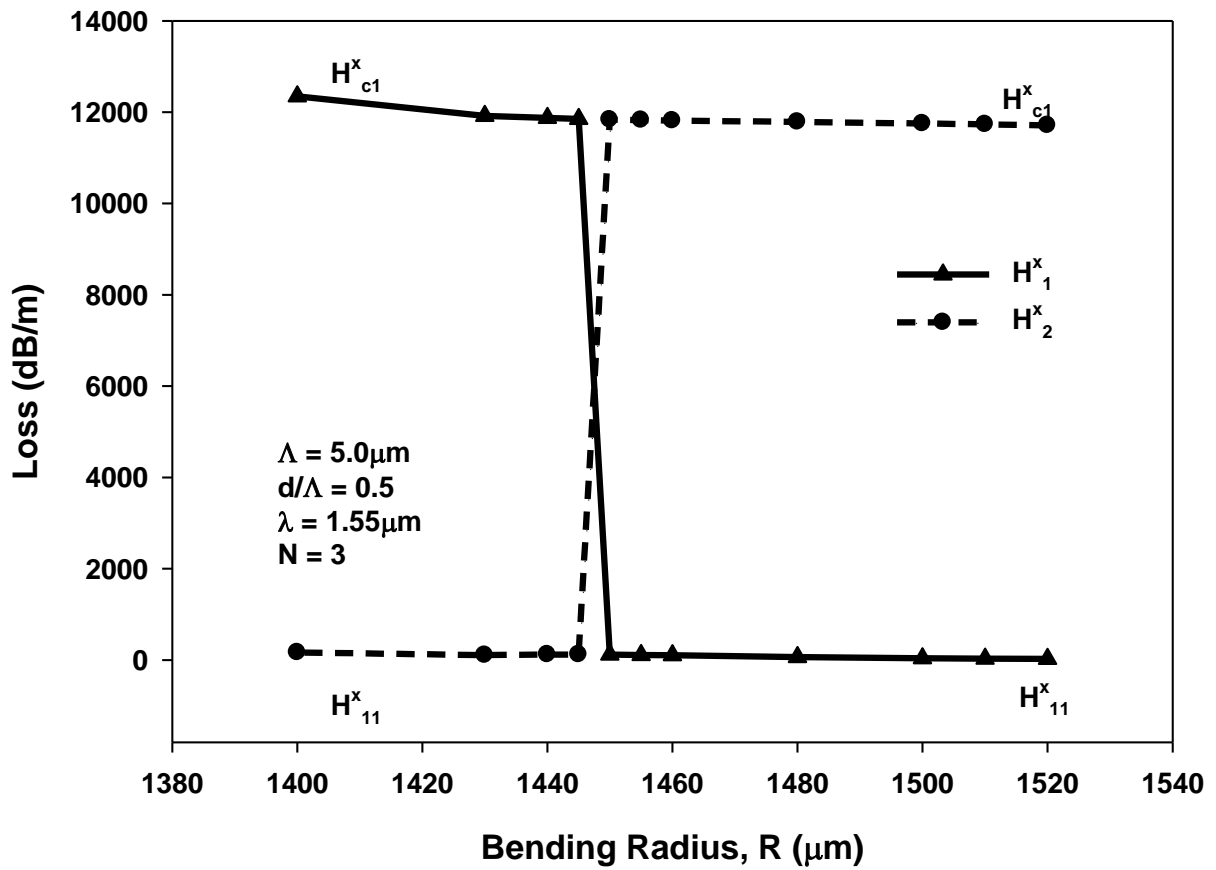


Fig. 3. Variation of the total losses with the bending radius, R.

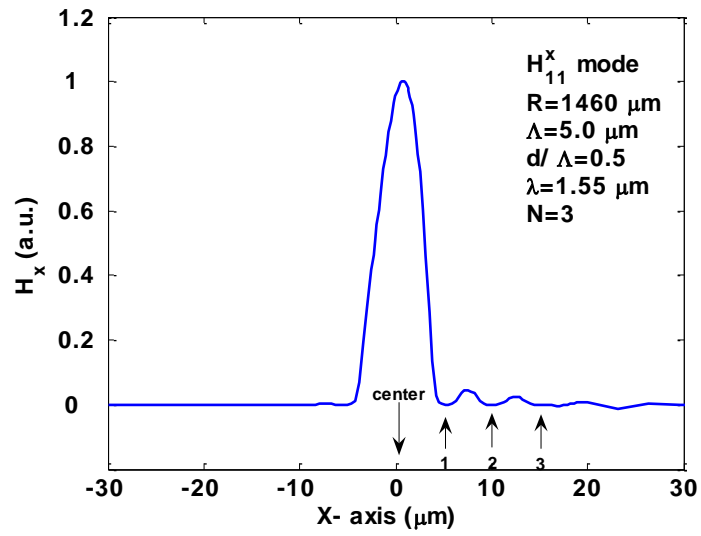


Fig. 4.  $H_x$  field profile of the  $H_{11}^x$  core mode along the X-axis through the center of the core, when  $R = 1460 \mu\text{m}$ .

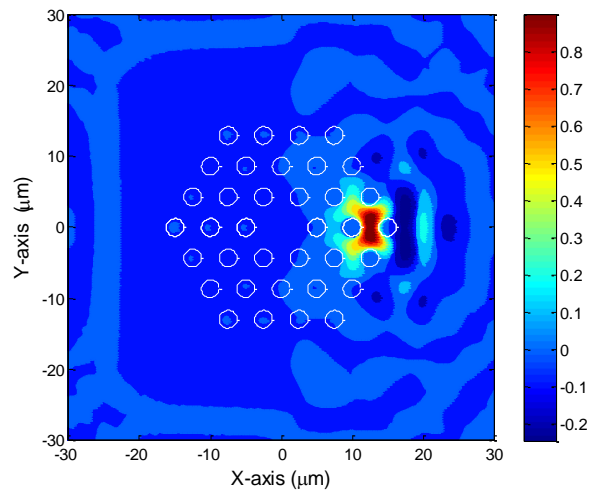


Fig. 5.  $H_x$  field contour for  $H_{c1}^x$  cladding mode when  $R = 1460 \mu\text{m}$ .

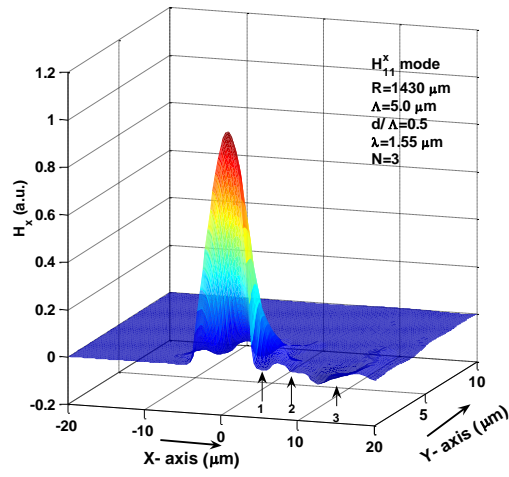


Fig. 6.  $H_x$  field profile for the  $H_{11}^x$  core mode, when  $R = 1430 \mu\text{m}$ .

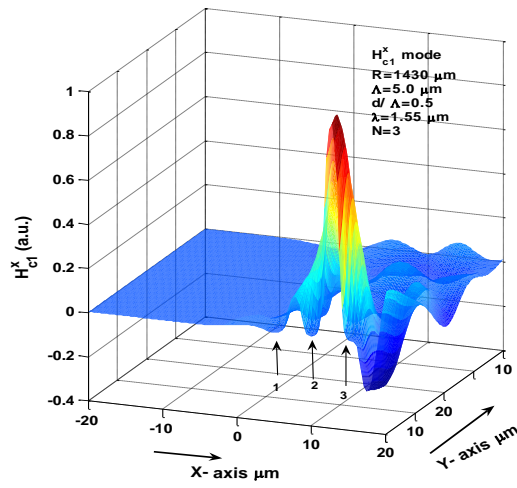


Fig.7.  $H_x$  field profile for the  $H_{c1}^x$  cladding mode when  $R = 1430 \mu\text{m}$ .

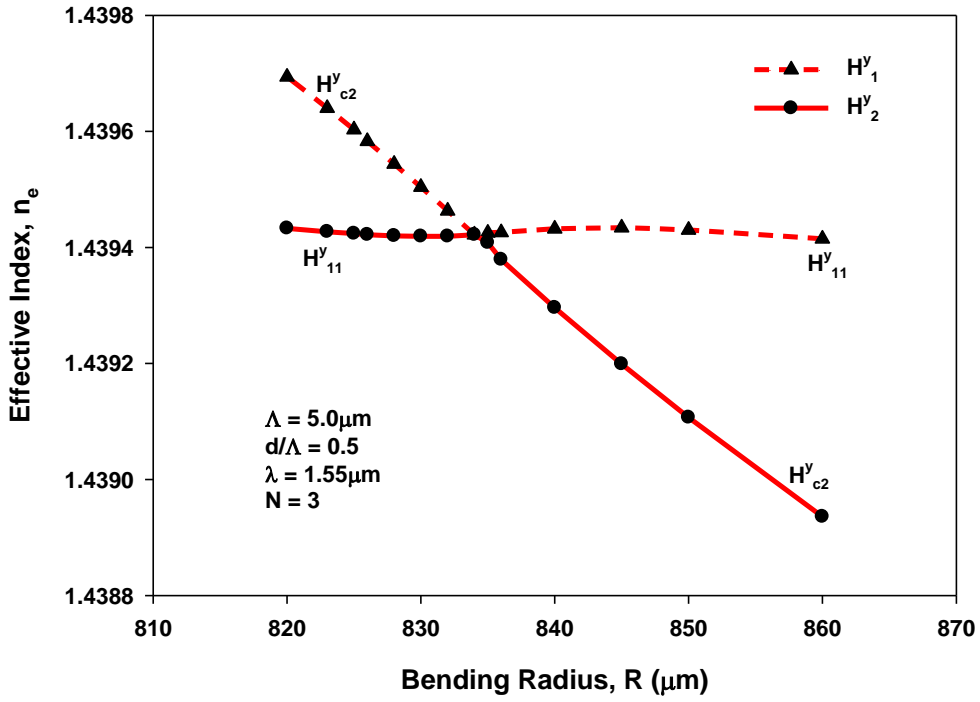


Fig. 8. Variation of the effective indices with the bending radius for the quasi-TE modes.

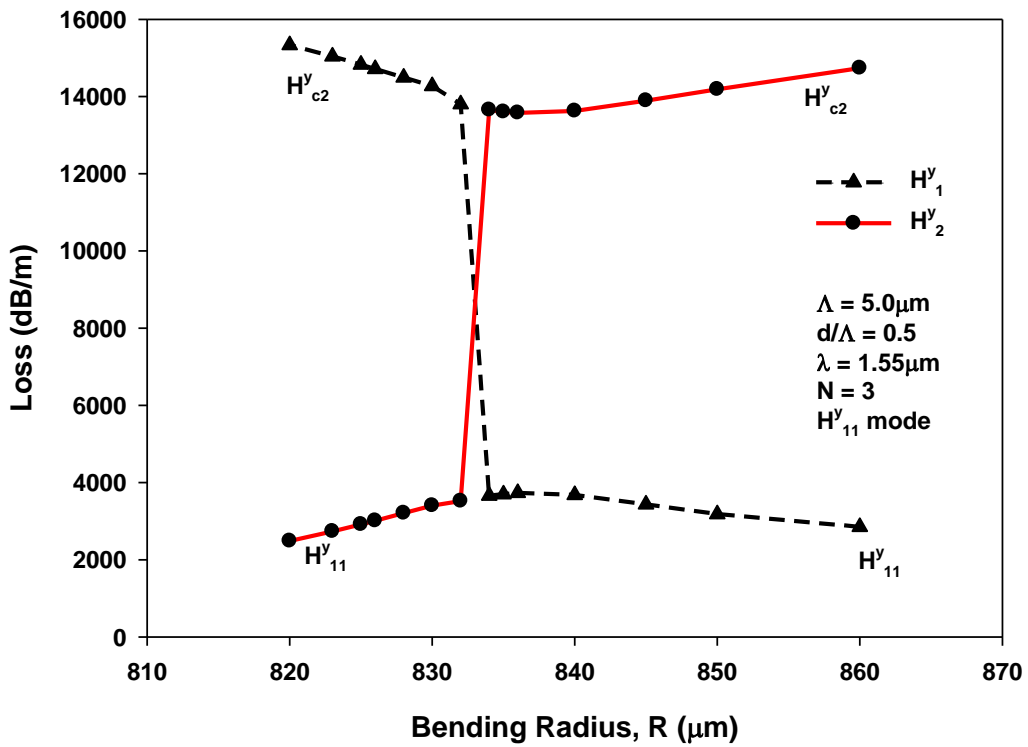


Fig. 9. Variation of the total losses with the bending radius, R

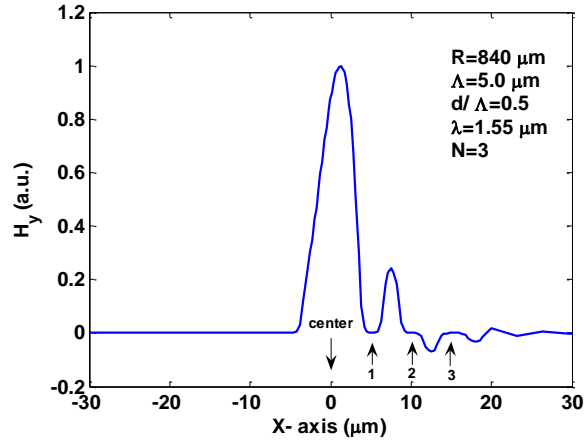


Fig. 10.  $H_y$  field profile along the X-axis for the  $H_{11}^y$  core mode, when  $R = 840 \mu\text{m}$ , above the degeneration point.

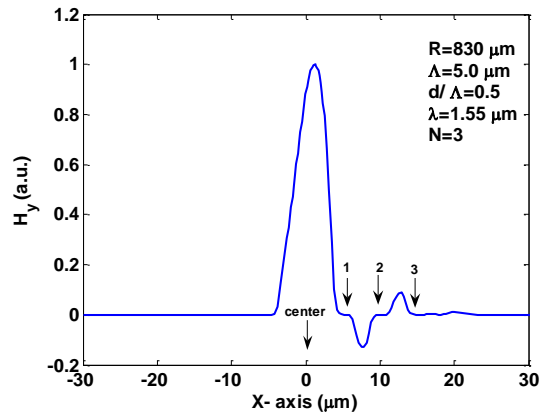


Fig. 11.  $H_y$  field profile along the X-axis for the  $H_{11}^y$  core, when  $R = 830 \mu\text{m}$ , below the degeneration point.



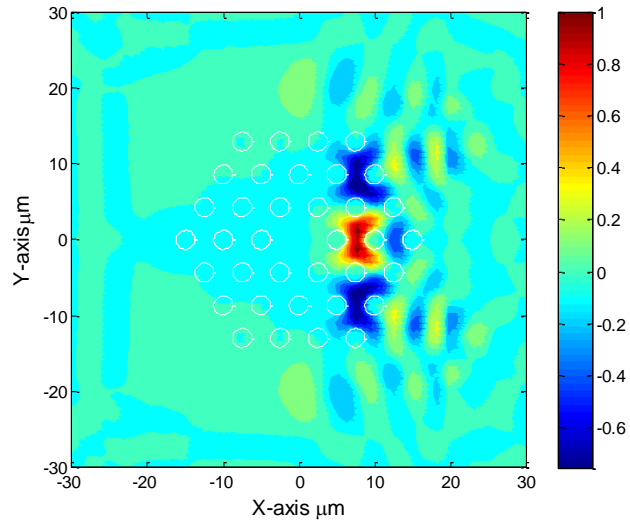


Fig. 12.  $H_y$  contour of the higher order cladding mode, when  $R = 833 \mu\text{m}$ .